ELSEVIER

Full paper/Mémoire

Exploring the coordination abilities of 1,5-diisopropyl-3-(4′-carboxyphenyl)-6-oxoverdazyl

Varun Kumar [a], Sergiu Shova [b, **], Ghenadie Novitchi [a, *], Cyrille Train [a]

[a] *Laboratoire national des champs magnétiques intenses—European Magnetic Field Laboratory, UPR3228 CNRS, Université Grenoble-Alpes, Grenoble, France*
[b] *"Petru Poni" Institute of Macromolecular Chemistry, Laboratory of Inorganic Polymers, Aleea Gr. Ghica Voda 41A, 700487, Iasi, Romania*

A B S T R A C T

The reactivity of 1,5-diisopropyl-3-(4′-carboxyphenyl)-6-oxoverdazyl H$\mathbf{I}_{i\text{-}Pr}$ toward divalent metal ions is dominated by the coordination of the carboxylate moiety onto the metal ions. The formula of the compound obtained by the reaction with the earth-alkaline magnesium (II) is $[Mg(\mathbf{I}_{i\text{-}Pr})_2 \cdot 2H_2O]_n \cdot 0.35H_2O$ ($\mathbf{I}_{i\text{-}Pr}$–Mg) whereas the reaction with 3d divalent metal ions yields compounds of general formula $[M(\mathbf{I}_{i\text{-}Pr})_2(CH_3OH)_4]$ (M = Mn ($\mathbf{I}_{i\text{-}Pr}$–Mn), Co ($\mathbf{I}_{i\text{-}Pr}$–Co), Ni ($\mathbf{I}_{i\text{-}Pr}$–Ni), Zn ($\mathbf{I}_{i\text{-}Pr}$–Zn)). The single-crystal X-ray diffraction analysis of $\mathbf{I}_{i\text{-}Pr}$–Mg reveals that the magnesium (II) adduct forms a one-dimensional (1D) coordination polymer with a terminal radical in a bidentate κ(O,O′) coordination mode and a bridging one in a μ − 1κ(O); 1κ (O′) *syn−anti* mode. The coordination sphere of the magnesium (II) is completed by two water molecules that established H-bonds with the carboxylate moiety of the terminal radicals that further reinforce the 1D coordination polymer. Adjacent chains interact through π-stacking of head-to-tail radicals. The single-crystal X-ray diffraction analysis of $\mathbf{I}_{i\text{-}Pr}$–Mn and $\mathbf{I}_{i\text{-}Pr}$–Ni reveals that the two compounds are isostructural. They are composed of mononuclear complexes where the divalent metal is surrounded by two radicals coordinated by monodentate carboxylate and four methanol molecules in the equatorial plane. Two methanol ligands act as H-bond donors toward the second oxygen atom of the carboxylate groups. The complexes interact through π-stacking of head-to-tail radicals and H-bonds between the two remaining methanol ligands and the oxygen atom of the oxoverdazyl moieties. In all of the compounds, the exchange interaction is dominated by the weak antiferromagnetic coupling related to the π-stacking of the radicals.

© 2019 Académie des sciences. Published by Elsevier Masson SAS. All rights reserved.

1. Introduction

Using radicals is an elegant although demanding strategy to develop highly coupled magnetic molecular systems. The radicals indeed benefit from the versatility of organic chemistry to introduce a welfare of chemical functions but suffer from stability problems. The latter phenomenon is more accurate when going from the nitronyl nitroxide radicals [1] used from the early stage of molecular magnetism to the more recently developed verdazyl radicals [2,3]. Given the strong exchange interaction found in some verdazyl-based systems [4,5] and their ability to coordinate lanthanide ions [6], it is necessary to find solutions to these problems to fully exploit the potential of verdazyl radicals.

A solution to the stability problem is the introduction of isopropyl side chain onto the radical moiety [7]. This bulky group stabilizes the radical and limits π-stacking

* Corresponding author.
** Corresponding author.
E-mail addresses: shova@icmpp.ro (S. Shova), ghenadie.novitchi@lncmi.cnrs.fr (G. Novitchi).

interaction that usually leads to rather strong antiferromagnetic interactions [8–10].

To test the possibility opened by such radicals, we have synthesized the 1,5-diisopropyl-3-(4′-carboxyphenyl)-6-oxoverdazyl [11]. Along these lines, we describe the reactivity of this radical toward divalent metal ions. The structures of three adducts determined by single-crystal X-ray diffraction (XRD) are detailed, whereas the magnetic properties of the five compounds that were obtained are described.

2. Experimental section

2.1. Synthesis

All chemicals were purchased from Sigma–Aldrich and were used as received.

HI_{i-Pr} verdazyl radicals have been prepared according to the procedure previously reported [11].

$[Mg(I_{i-Pr})_2 \cdot 2H_2O]_n \cdot 0.35H_2O$ (I_{i-Pr}–Mg): 0.1 g (0.33 mmol) of verdazyl radical HI_{i-Pr} was dissolved in 15.0 mL of methanol. To this solution was added an excess amount 0.5 g (8.6 mmol) of freshly prepared $Mg(OH)_2$. The reaction mixture was stirred for 30 minutes, filtered, and the solution was allowed to crystallize. These crystals were further recrystallized from ethyl acetate to give homogeneous and pure crystals of I_{i-Pr}–Mg. The compound was characterized by elemental analysis, IR spectroscopy, and single-crystal XRD. Yield (%) 61, Elemental analyses. Anal. Calcd for $C_{30}H_{40.7}MgN_8O_{8.35}$ ($M_r = 671.3$): C, 53.68; H, 6.11; N, 16.69. Found: C, 52.57; H, 6.08; N, 16.19. IR (cm^{-1}): 483, 546, 657, 667, 711, 794, 1167, 1230, 1369, 1387, 1410, 1456, 1539, 1558, 1611, 1652, 2982, 3446.

$[Mn(I_{i-Pr})_2(CH_3OH)_4]$ (I_{i-Pr}–Mn): 0.1 g (0.4 mmol) of manganese (II) acetate tetrahydrate was dissolved in 5.0 mL of methanol. To this solution was added a solution of 0.24 g (0.8 mmol) of HI_{i-Pr} in 15.0 mL of methanol. To this reaction mixture was added 20.0 mL of toluene. The resulting reaction mixture was stirred for 3 hours and thereafter was concentrated under reduced pressure. Toluene (20.0 mL) was added to the concentrated solution and stirred for another 3 hours. All of the solvent was evaporated under reduced pressure and the obtained microcrystalline product was recrystallized from methanol to yield red crystals of Mn(II)-verdazyl compound. These crystals were characterized by elemental analysis, IR spectroscopy, and single-crystal XRD. Yield (%) 57, Anal. Calcd for $C_{34}H_{52}N_8MnO_{10}$ ($M_r = 787.32$): C, 51.84; H, 6.65; N, 14.22. Found: C, 51.41; H, 6.57; N, 14.33. IR (cm^{-1}): 481, 656, 710, 791, 1168, 1229, 1370, 1387, 1404, 1456, 1545, 1610, 1684, 2978, 3416.

$[Zn(I_{i-Pr})_2(CH_3OH)_4]$ (I_{i-Pr}–Zn): the zinc(II) analogue I_{i-Pr}–Zn was obtained using the same procedure as for I_{i-Pr}–Mn but the crystals were not suitable for single-crystal XRD. Yield (%) 48.2, Anal. Calcd for $C_{34}H_{52}N_8O_{10}Zn$ ($M_r = 796.31$): C, 51.16; H, 6.57; N, 14.04. Found: C, 51.27; H, 6.37; N, 14.70. IR(cm^{-1}): 484, 546, 656, 710, 790, 871, 1018, 1128, 1168, 1229, 1301, 1368, 1386, 1557, 1610, 1685, 2934, 2978, 3419.

$[Ni(I_{i-Pr})_2(CH_3OH)_4]$ (I_{i-Pr}–Ni): 0.1 g (0.4 mmol) of nickel (II) acetate tetrahydrate was dissolved in 5.0 mL of methanol. To this solution was added a solution of 0.24 g (0.8 mmol) of HI_{i-Pr} in 15.0 mL of methanol. The resulting reaction mixture was stirred for 20 minutes and allowed to crystallize to yield small crystals of I_{i-Pr}–Ni. These crystals were characterized by elemental analysis, IR spectroscopy and single-crystal XRD. IR spectrum is given in Annexure. Yield (%) 55, Anal. Calcd for $C_{34}H_{52}N_8NiO_{10}$ ($M_r = 790.32$): C, 51.59; H, 6.62; N, 14.16. Found: C, 50.49; H, 6.57; N, 14.32. IR (cm^{-1}): 657, 710, 789, 1018, 1168, 1229, 1369, 1387, 1550, 1610, 1685, 2979, 3420.

$[Co(I_{i-Pr})_2(CH_3OH)_4]$ (I_{i-Pr}–Co): the cobalt (II) analogue I_{i-Pr}–Co was obtained using the same procedure as for I_{i-Pr}–Ni but the crystals were not suitable for single-crystal XRD. Yield (%) 68, Elemental analyses. Anal. Calcd for $C_{34}H_{52}N_8O_{10}Co$ ($M_r = 791.31$): C, 51.58; H, 6.62; N, 14.15. Found: C, 51.69; H, 6.43; N, 14.24. IR (cm^{-1}): 485, 547, 657, 711, 789, 871, 1018, 1168, 1229, 1369, 1387, 1558, 1610, 1685, 2978, 3420.

2.2. Physical measurements and instrumentation

Elemental analyses were carried out at the Microanalytical Service of the Faculty of Chemistry of the Grenoble University. IR spectra were measured using a Nicolet iS50FTIR spectrometer in KBr.

2.3. Crystallographic structure determination

Crystallographic measurements for compounds I_{i-Pr}–Mg, I_{i-Pr}–Mn, I_{i-Pr}–Ni were carried out using an Oxford-Diffraction Xcalibur E charge-coupled device (CCD) diffractometer equipped with graphite-monochromated Mo Kα radiation. The crystals were placed 40 mm from the CCD detector. The unit cell determination and data integration were carried out using the CrysAlis package of Oxford Diffraction [12]. The structure was solved by direct methods using Olex2 [13] software with the SHELXS [14] structure solution program and refined by full-matrix least-squares on F_0^2 with SHELXL-2015 [14]. Atomic displacements for non-hydrogen, nondisordered atoms were refined using an anisotropic model. For I_{i-Pr}–Mg, which crystallizes in Sohnke $C2$, space group inversion twinning was checked by the refinement of BASF parameter (the BASF is the refined parameter which indicates the twin component ratio); however, the value of −0.1 (4) for the Flack gave no conclusive answer. In addition, the "Solvent Mask" tool available in Olex2 was used to model the contribution of disordered solvent molecules to structure factors. The hydrogen atoms have been placed by Fourier Difference accounting for the hybridization of the supporting atoms and the possible presence of hydrogen bonds in the case of donor atoms. The molecular plots were obtained using the Olex2 program [13]. The main crystallographic data together with refinement details are summarized in Table 1, whereas the selected bond lengths and angles are presented in Table 2.

CCDC-1892270 for I_{i-Pr}–Mg, CCDC-1892067 for I_{i-Pr}–Ni, and 1892068 for I_{i-Pr}–Mn contain the supplementary crystallographic data for this article; these data can be obtained free of charge via http://www.ccdc.cam.ac.uk/conts/retrieving.html.

The powder XRD experiment at room temperature was performed on a D8 Advance Bruker AXS diffractometer using a Cu Kα source with an emission current of 36 mA and

Table 1
Crystallographic data, details of data collection, and structure refinement parameters for the investigated compounds.

	I$_{i\text{-Pr}}$–Mg	I$_{i\text{-Pr}}$–Ni	I$_{i\text{-Pr}}$–Mn
Empirical formula	C$_{30}$H$_{40.7}$MgN$_8$O$_{8.35}$	C$_{34}$H$_{52}$N$_8$NiO$_{10}$	C$_{34}$H$_{52}$MnN$_8$O$_{10}$
Formula weight	671.31	791.54	787.77
Temperature (K)	200	200	293
Crystal system	Monoclinic	Monoclinic	Monoclinic
Space group	$C2$	$P2_1/n$	$P2_1/n$
a (Å)	27.2230 (10)	9.1932 (4)	9.1746 (8)
b (Å)	9.4380 (3)	14.1686 (5)	14.4667 (15)
c (Å)	15.4136 (6)	15.1827 (6)	15.3873 (8)
α(°)	90.00	90.00	90.00
β(°)	104.751 (4)	94.809 (3)	93.480 (6)
γ(°)	90.00	90.00	90.00
V (/Å^3)	3829.7 (2)	1970.67 (13)	2038.5 (3)
Z	4	2	2
D_{calc} (/mg/mm^3)	1.164	1.334	1.283
μ (mm^{-1})	0.101	0.556	0.385
Crystal size (/mm^3)	0.10 × 0.10 × 0.35	0.10 × 0.15 × 0.20	0.05 × 0.15 × 0.40
θ_{min}, θ_{max} (°)	5.536–50.048	3.938–50.052	3.868–50.046
Reflections collected	13,980	9548	8634
Independent reflections	6745 [R_{int} = 0.0359]	3459 [R_{int} = 0.0239]	3582 [R_{int} = 0.0356]
Data/restraints/parameters	6745/2/465	3459/4/247	3582/7/235
R_1[a] ($I > 2\sigma(I)$)	0.0489	0.0348	0.0589
wR_2[b] (all data)	0.0924	0.0849	0.1537
GOF[c]	0.991	1.081	1.0394
Flack parameter	−0.1 (4)	—	—
$\Delta\rho_{max}$ and $\Delta\rho_{min}$ (e/Å^3)	0.29/−0.26	0.30/−0.24	0.32/−0.38

[a] $R_1 = \Sigma||F_o|-|F_c||/\Sigma|F_o|$.
[b] $wR_2 = \{\sum[w\,(F_o^2 - F_c^2)^2]/\sum[w(F_o^2)^2]\}^{1/2}$.
[c] GOF $= \{\sum[w(F_o^2 - F_c^2)^2]/(n-p)\}^{1/2}$, where n is the number of reflections and p is the total number of parameters refined.

Table 2
Selected bond lengths (Å).

Distance	H^{a}I$_{i\text{-Pr}}$[11]	I$_{i\text{-Pr}}$–Mg M = Mg		I$_{i\text{-Pr}}$–Ni M = Ni	I$_{i\text{-Pr}}$–Mn M = Mn
		A	B		
C1–O1	1.326 (2)	1.249 (4)	1.256 (4)	1.261 (2)	1.262 (4)
C1–O2	1.210 (2)	1.263 (6)	1.252 (6)	1.252 (2)	1.247 (4)
C1–C2	1.491 (2)	1.487 (5)	1.498 (5)	1.512 (3)	1.506 (4)
C2–C3	1.387 (2)	1.409 (5)	1.377 (5)	1.383 (3)	1.386 (4)
C3–C4	1.378 (2)	1.382 (5)	1.398 (5)	1.386 (3)	1.373 (4)
C4–C5	1.393 (2)	1.394 (5)	1.389 (5)	1.388 (3)	1.378 (3)
C5–C6	1.391 (2)	1.400 (5)	1.381 (5)	1.389 (3)	1.383 (4)
C5–C8	1.488 (2)	1.477 (5)	1.486 (5)	1.486 (3)	1.484 (4)
C6–C7	1.381 (2)	1.384 (6)	1.387 (5)	1.383 (3)	1.386(4)
C7–C2	1.392 (2)	1.383(5)	1.384 (5)	1.389 (3)	1.382(3)
C8–N3	1.333 (2)	1.324 (5)	1.325 (5)	1.326 (2)	1.340 (4)
N3–N2	1.367 (2)	1.365 (4)	1.363 (4)	1.368(2)	1.363 (3)
N2–C9	1.369 (2)	1.376 (5)	1.371 (5)	1.373 (2)	1.363 (3)
N2–C10	1.484 (2)	1.482 (5)	1.498 (5)	1.478 (3)	1.477 (4)
C9–O3	1.231 (2)	1.225 (4)	1.224 (4)	1.230 (2)	1.231 (3)
C9–N1	1.369 (2)	1.380 (5)	1.370 (5)	1.371 (3)	1.371 (4)
N4–C8	1.326 (2)	1.316 (5)	1.332 (5)	1.331 (2)	1.321 (4)
N1–N4	1.367 (2)	1.357 (4)	1.365 (4)	1.362 (2)	1.367 (3)
N1–C11	1.481 (2)	1.495 (5)	1.489 (5)	1.478 (2)	1.472 (4)
C10–C12	1.509 (2)	1.504 (7)	1.500 (6)	1.513 (3)	1.509 (5)
C10–C13	1.509 (2)	1.520 (6)	1.478 (6)	1.506 (3)	1.493 (5)
C11–C14	1.520 (3)	1.492 (7)	1.440 (11)	1.508 (3)	1.500 (5)
C11–C15	1.505 (3)	1.510 (7)	1.453 (7)	1.504 (3)	1.501 (5)
C16–O4				1.412 (3)	1.371 (6)
C17–O5				1.426 (3)	1.312 (6)
M1–O1		2.199 (3)	2.035 (3)	2.0306 (13)	2.1169 (19)
M1–O2		2.139 (3)	2.027 (3)^i		
M1–O4				2.0651 (13)	2.254 (4)
M1–O5				2.0815 (13)	2.178 (4)
M1–O1w		2.025 (4)			
M1–O2w		2.0346 (3)			

Symmetry code $^{(i)}$0.5 − x, 0.5 +y, −z.

a voltage of 30 kV. Scans were collected over the $2\theta = 5-45$ range using a step size of 0.01° and a count time of 0.5 s/step.

2.4. Magnetism studies

Magnetic measurements were carried out on microcrystalline samples with a Quantum Design SQUID magnetometer (MPMS-XL). Variable-temperature (2–300 K) direct current magnetic susceptibility was measured under an applied magnetic field of 0.1 T. All data were corrected for the contribution of the sample holder and diamagnetism of the samples estimated from Pascal's constants [15,16]. The analysis of the magnetic data was carried out by fitting the χT and χ thermal variations including temperature-independent paramagnetism, impurity contribution (ρ), and intermolecular interaction (zJ') [16–18].

3. Results and discussion

3.1. Synthesis

The chemistry of HI$_{i\text{-Pr}}$ with a bivalent metal is explored. I$_{i\text{-Pr}}$–Mg was obtained by reacting HI$_{i\text{-Pr}}$ with an excess of freshly prepared Mg(OH)$_2$ in methanol according to the following reaction:

$$Mg(OH)_2 + 2HI_{i\text{-Pr}} \leftrightarrow Mg(I_{i\text{-Pr}})_2 + 2H_2O$$
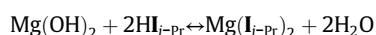
After filtration, methanol was evaporated and crystals suitable for XRD were grown from ethyl acetate.

For the 3d bivalent metal ions (Mn(II), Co(II), Ni(II), and Zn(II)), the starting materials were the hydrates of the metal (II) acetate. The overall reaction toward the final compounds thus appears as a substitution of the acetate ions by the carboxylate moiety of I_{i-Pr}^- according to the following reaction:

$$M(Ac)_2 + 2HI_{i-Pr} \leftrightarrow M(I_{i-Pr})_2 + 2HAc \quad M(II) = Mn, Co, Ni, Zn$$
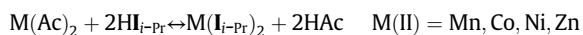
In the case of Co(II) and Ni(II) (I_{i-Pr}–Co and I_{i-Pr}–Ni), a direct substitution of acetic acid in methanol solution was performed. On the contrary, for Mn(II) and Zn(II), it is necessary to displace the equilibrium toward the desired compounds, I_{i-Pr}–Mn and I_{i-Pr}–Zn, by a double azeotropic distillation of acetic acid in toluene. This procedure is similar to the one used to vary the nature of the carboxylate in Mn_{12} derivatives [19]. It should be noted that an analogous synthesis was undertaken starting from iron (II) and copper (II) acetate. Nonetheless, the redox activity of these metal ions toward verdazyl radicals [7,10] has modified the overall reaction scheme and prevented the synthesis of the

corresponding analogues. According to X-ray analysis, the magnesium salt contains two coordination molecules of water.

Elemental analysis is in good agreement with the proposed composition, but in the case of Mg salt, some discrepancy may be observed, which probably can be associated with solvent loss before analysis. The IR spectra of all the 3d divalent metal ion derivatives I_{i-Pr}–M (M = Mn, Co, Ni, Zn; Fig. SI 1) are very similar and markedly different from that of the magnesium (II) derivatives I_{i-Pr}–Mg (Fig. SI 2). This strongly suggests that the composition and bond repartitions are similar within the I_{i-Pr}–M (M = Mn, Co, Ni, Zn) series and notably different in I_{i-Pr}–Mg. Several features in the IR spectra of the synthesized compounds compared with that of the starting radical HI_{i-Pr} can be detailed (Fig. SI 3). First, the fingerprint of the organic part of HI_{i-Pr} is retrieved in all of the five derivatives. On the contrary, significant differences appear in the vibrations associated with the carboxylate moiety of the radical. Upon deprotonation and complexation, the characteristic band of OH vibration is deeply modified because in HI_{i-Pr} the molecules form H-bonded dimers that forced the O-H bond, hence displaced the OH vibration down to 2680–2550 cm^{-1} whereas the O-H bonds of the water and methanol molecules present in the
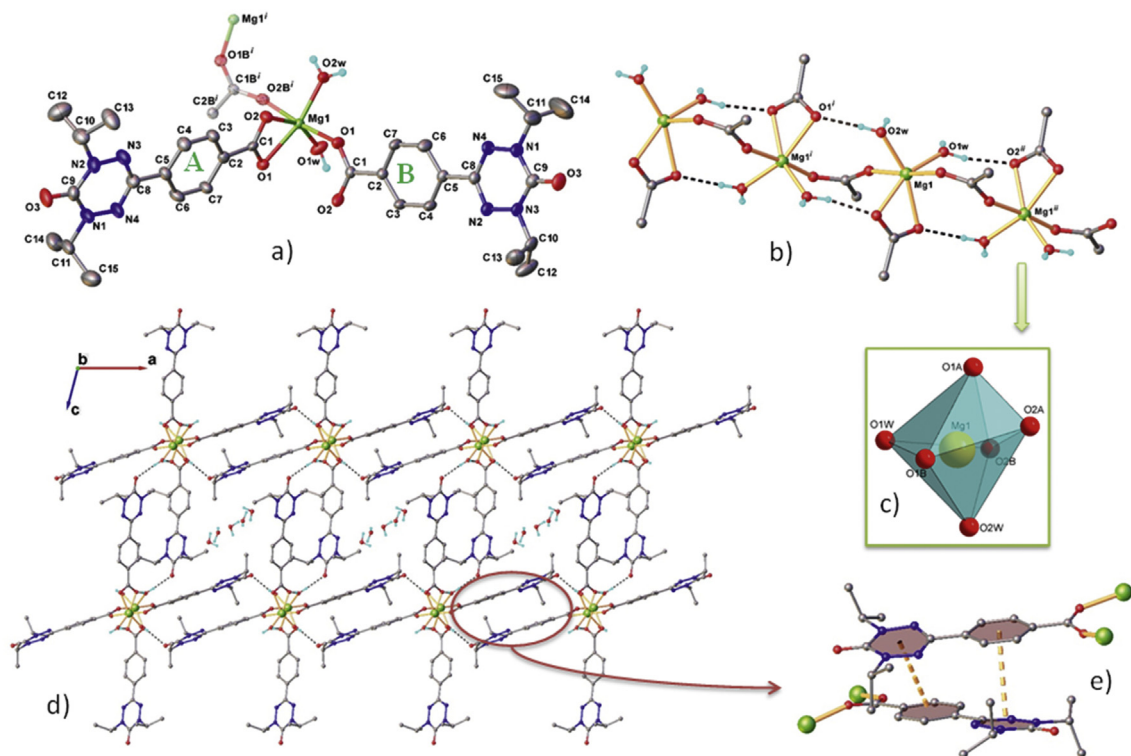

Fig. 1. The crystal structure of compound I_{i-Pr}–Mg. (a) Extended view of the asymmetric part and coordination environment around Mg^{2+} along with the atom labeling scheme and thermal ellipsoids the 50% probability level. Two radical ligands are denoted as A and B. Symmetry generated fragments are shown with faded colors. Symmetry codes: $^{(i)}$−0.5 − x, 0.5 + y, −z; (b) fragment of 1D polymer chain, intrachain H-bonds as dashed lines: O1w–H···O2A [O1w–H 0.86 Å, H···O2A 1.91 Å, O1w···O2A (−x, +0.5, y − 0.5, −z) 2.758 Å, ∠ O1w–H···O2A 160.0°], O2w–H···O1A [O2w–H 0.85 Å, H···O1A 1.84 Å, O2w···O1A (−x, +0.5, y + 0.5, −z) 2.685 Å, ∠ O2wHO1A 177.2°]; (c) coordination polyhedron of Mg(II); (d) crystal packing viewed along the b axis; and (e) closer view at π−π stacking between two B radical ligands.

divalent metal adducts, $\mathbf{I}_{i\text{-Pr}}$–M, vibrate at much higher wavenumbers, for example, 3420 cm^{-1}, indicating the presence of much less efficient H-bonding. Another striking consequence of the coordination is the modification of ν_{as} (COO) and ν_s (COO), respectively, the asymmetrical and symmetrical carboxylate oscillation bands. The difference between the two bands $\Delta\nu = \nu_{as}$ (COO) − ν_s (COO) takes value from (1680−1404) 282 cm^{-1} in $\mathbf{I}_{i\text{-Pr}}$–Mn down to (1652−1410) 242 cm^{-1} when the carboxylate moiety adopts a pseudobidentate coordination ($\mathbf{I}_{i\text{-Pr}}$–Mg). These results indicate that the verdazyl moiety itself shall

not be coordinated whereas the carboxylate moiety does. These results must be compared with those obtained by the single-crystal X-ray structural analysis.

3.2. X-ray diffraction

Fig. 1(a) shows the asymmetric unit of $\mathbf{I}_{i\text{-Pr}}$–Mg. Two different modes of coordination of the radical to magnesium (II) are found in $\mathbf{I}_{i\text{-Pr}}$–Mg. They are denoted as A and B. One radical is coordinated to Mg(II) by its carboxylate group in a bidentate $\kappa(O,O')$ coordination mode (A). The

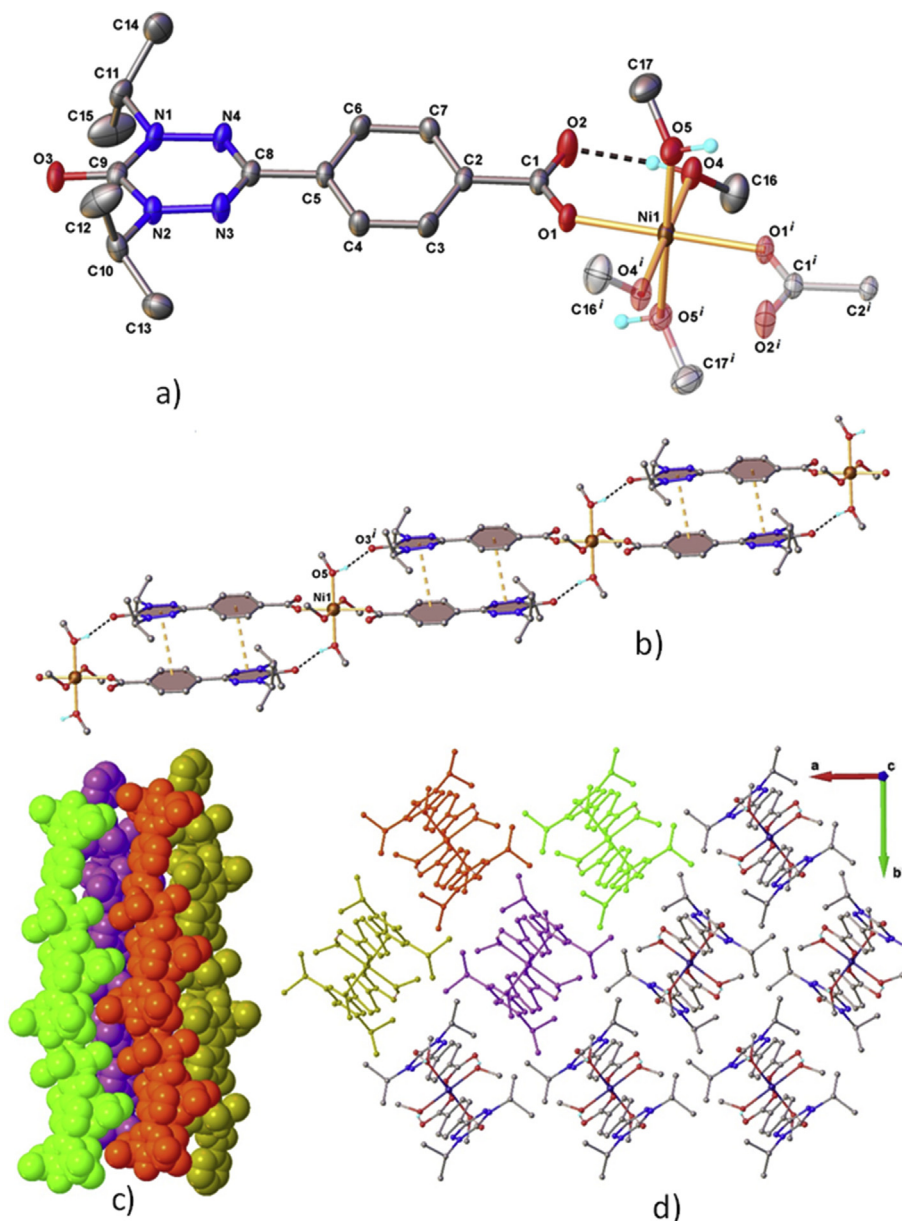**Fig. 2.** Crystal structure of $\mathbf{I}_{i\text{-Pr}}$–Ni.A) Extended view of the asymmetric part and coordination environment around Ni^{2+} along with the atom labeling scheme and thermal ellipsoids the 50% probability level. Symmetry generated fragments are shown with faded colors. Symmetry codes: $^{(i)}$1 − x, 1 − y, −z; (b) the supramolecular chain of π−π stacking and hydrogen bonds: O4-H···O2 [O4-H 0.85 Å, H···O2 1.76 Å, O4···O2 2.589 (2), ∠O4HO2 165.1°, O5-H···O3 [O5-H 0.84 Å, H···O3 1.90 Å, O5···O3(x, y, −1 + z) 2.722 (2), ∠O5HO3 164.3°; (c) and (d) the packing of 1D discrete chains along the c axis.

second radical is coordinated in a $\mu - 1\kappa(O); 1\kappa(O')$ *syn−anti* mode (B): one oxygen atom (O1B) is coordinated to Mg1 atom (Mg1-O1B = 2.031 Å) whereas the second oxygen atom of the carboxylate group (O2B) is connected to another, crystallographically equivalent, Mg atom (O2B-Mg1 = 2.037 Å). These bridges between the Mg(II) ions lead to the formation a one-dimensional (1D) coordination polymer (Fig. 1b).

The coordination sphere of the metal ion is completed by two water molecules leading to a highly distorted octahedral environment (Fig. 1c). The two intrachain hydrogen bonds between the coordinated water molecules and the bidentate radical further reinforce the 1D chain. Fig. 1(d) shows the crystal packing of the coordinated polymer. There is no π-stacking between the molecules of bidentate chelating radicals A. On the contrary, there are some π−π interactions between bridging ligands B. Fig. 1e shows that the stacking is far from being perfect because of both the bulkiness of the isopropyl groups borne by the verdazyl moieties and to the coordinated magnesium (II) ions onto the carboxylate groups. Centroid-to-centroid distance is of 3.911 and 5.613 (Å) for phenyl−verdazyl and verdazyl−verdazyl pairs, respectively, and angle between two stacked molecules equal to 18.7°(2).

$\mathbf{I}_{i\text{-Pr}}$−Mn and $\mathbf{I}_{i\text{-Pr}}$−Ni are isostructural (Table 1). The structure of the latter is presented in detail in Fig. 2. This compound is formed of isolated mononuclear complexes. In the complex, the nickel (II) ion is coordinated by four methanol molecules and two radicals (Fig. 2a). The two radicals are coordinated to the metal ion by the carboxylate group in a monodentate mode. The second oxygen atoms of the two carboxylate groups (O2) are engaged in an intramolecular hydrogen bond with the hydrogen atoms (H4) of two coordinated methanol molecules. The two remaining methanol ligands form additional hydrogen bonds with oxygen atoms of the carbonyl groups of a verdazyl ring (Fig. 2b). The intermolecular interactions between the neighboring complexes are reinforced by π-stacking between the organic parts of the radicals arranged in a head-to-tail configuration (Fig. 2b). Centroid-to-centroid distance is of 3.940 for phenyl−verdazyl and 6.069 (Å) verdazyl−verdazyl pairs, respectively. These two intermolecular interactions lead to the formation of well-isolated 1D chain of complexes, which propagate along the *c*-axis (Fig. 2c and d).

The structure of the mononuclear complexes observed in $\mathbf{I}_{i\text{-Pr}}$−Mn and $\mathbf{I}_{i\text{-Pr}}$−Ni is very similar to that of the [M(OOCCH$_3$)$_2$(H$_2$O)$_4$] [20] supporting the substitution scenario proposed for the reaction. On the basis of the similarity of the IR spectra of $\mathbf{I}_{i\text{-Pr}}$−Mn, $\mathbf{I}_{i\text{-Pr}}$−Co, $\mathbf{I}_{i\text{-Pr}}$−Ni, and $\mathbf{I}_{i\text{-Pr}}$−Zn, as well and on the powder XRD (see Supplementary Information), this scenario should hold for $\mathbf{I}_{i\text{-Pr}}$−Co and $\mathbf{I}_{i\text{-Pr}}$−Zn.

3.3. Magnetic properties

Fig. 3 shows the temperature variation of magnetic susceptibility of $\mathbf{I}_{i\text{-Pr}}$−Mg. The $\chi_M T$ product is worth 0.72 cm^3 mol^{-1} K at room temperature. This is close to the value expected for the sum of two noninteracting radicals (0.75 cm^3 mol^{-1} K for $g = 2.00$). Upon cooling, the $\chi_M T$
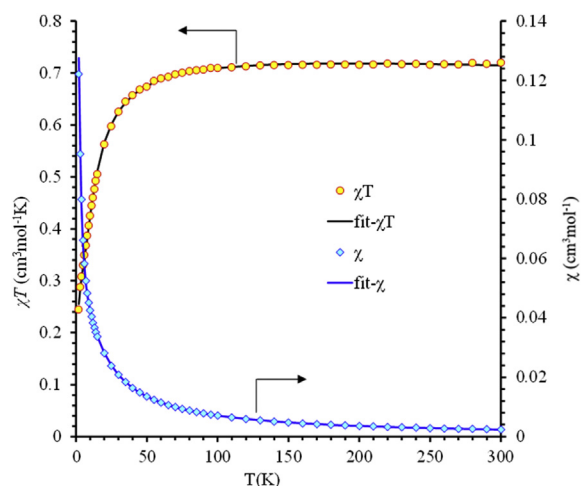

Fig. 3. Thermal variations of χ_M and $\chi_M T$ of $\mathbf{I}_{i\text{-Pr}}$−Mg. Solid lines represent the best fit according to the model given in the text.

product decreases continuously with an increasing rate when the temperature is decreased. This evolution indicates that the exchange interactions between the two spin bearers are dominated by antiferromagnetic interactions.

With this diamagnetic metal ion, exchange interaction should mainly originate from π−π interactions between the radicals. Following the structure analysis of $\mathbf{I}_{i\text{-Pr}}$−Mg (Fig. 1), such interactions exist between radicals labeled B whereas the A radicals are not coupled. Accordingly, the magnetic susceptibility is fitted using the following equation:
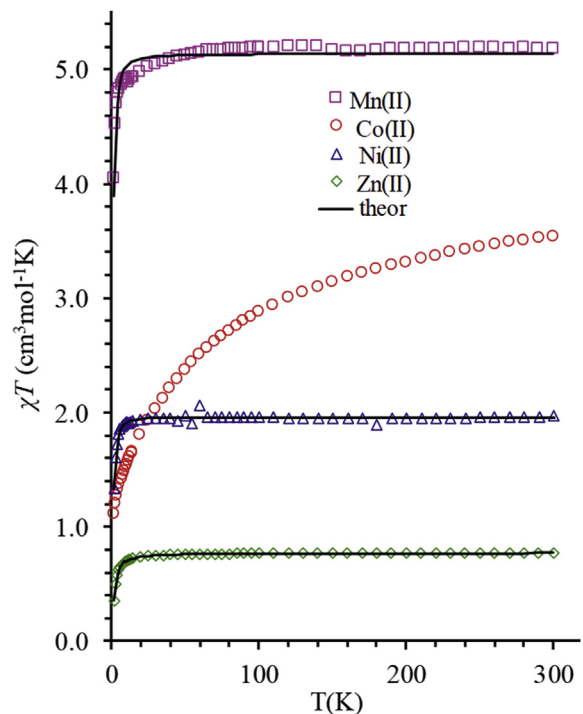

Fig. 4. Thermal variations of χT product for $\mathbf{I}_{i\text{-Pr}}$−M (M = Mn, Co, Ni, and Zn). Solid lines represent the best fits according to the model given in the text.

Table 3
Characteristic parameters for the series $I_{i\text{-}Pr}$−M (M = Mg, Mn, Co, Ni, Zn) extracted from the fit of the magnetic data.

$I_{i\text{-}Pr}$−M	χT (300 K) (exp)	S_M	g_R	g_{Met}	J	R	ZFS
Mg(II)		0	1.960 (2)	−	−17.6 (2)	3×10^{-4}	
Zn(II)	0.771	0	2.030 (1)	−	−2.40 (2)	6.6×10^{-6}	
Ni(II)	1.968	1	2.0 (fix)	2.20 (3)	−1.98 (8)	1.5×10^{-2}	D=−4.37 (3),
Co(II)	3.539	3/2	−	−	−	−	
Mn(II)	5.179	5/2	2.0 (fix)	2.003 (7)	−2.2 (4)	8×10^{-3}	

$$\chi(T) = \frac{1}{2}\left[\frac{2Ng^2\beta^2}{k_BT} \times \frac{1}{3 + e^{-J/k_BT}} + 2\frac{Ng^2\beta^2}{3k_BT}S_R(S_R + 1)\right]$$

where the first term ascribes for the π-stacked dimers following a classical Bleaney−Bowers coupling scheme (H = $-JS_1S_2$ with $S_1 = S_2 = 1/2$) [16,21], and the second term is a Curie law accounting for the contribution of the isolated radicals ($S_R = 1/2$).

From fitting the value of antiferromagnetic coupling constant was found to be $J = -17.56$ cm^{-1} and $g = 1.96$ (2). The low value of the g factor, as compared with the one expected for an organic radical, is probably due to the presence of a diamagnetic amorphous impurity. The constant of intermolecular interaction is -0.68 (1) cm^{-1}.

The thermal variations of χT product for the series of 3d series compounds $I_{i\text{-}Pr}$−M (M = Mn(II), Co(II), Ni(II), Zn(II)) is presented in Fig. 4. The values at the room temperature are consistent with theoretical value expected for two independent radical and one bivalent metal ion. Upon cooling, the χT products undergo a monotonous decrease. For $I_{i\text{-}Pr}$−Mn, $I_{i\text{-}Pr}$−Ni, and $I_{i\text{-}Pr}$−Zn, this temperature dependence suggests the presence of antiferromagnetic interaction whereas the much marked evolution for $I_{i\text{-}Pr}$−Co is a characteristic trademark of the strong spin orbital contribution of the octahedral Co(II) ion. Given that the radical is coordinated through its carboxylate, hence the long distance between the radical and the metal ion, and the similarity of the structure (Fig. 2) and thermal dependence of the χT products (Fig. 4) for $I_{i\text{-}Pr}$−Mn, $I_{i\text{-}Pr}$−Ni, and $I_{i\text{-}Pr}$−Zn, it clearly appears that the exchange interaction mainly originates from the π-stacking of the verdazyl moieties (Fig. 2b). Accordingly, the magnetic susceptibility data for $I_{i\text{-}Pr}$−M (M = Mn(II), Co(II), Ni(II), Zn(II)) can be written as

$$\chi(T) = \chi_d(T) + \chi_M(T)$$

where $\chi_d(T)$ is the susceptibility for the π-stacked dimers following a classical Bleaney−Bowers coupling scheme (H = $-JS_1S_2$ with $S_1 = S_2 = 1/2$) [16,21] and $\chi_M(T)$ is the paramagnetic susceptibility of an isolated metal center (M= Mn(II), Co(II), Ni(II), Zn(II)). For the diamagnetic zinc(II), this latter contribution has been omitted. For the isotropic Mn(II), $\chi_{Mn}(T)$ follows the Curie law. For the anisotropic nickel (II) compound, the zero field splitting (ZFS) parameter was first determined by the simultaneous fit of the field of the magnetization at 2, 3, 4, and 5 K (Fig. SI 4). The obtained parameters were taken into account to calculate $\chi_{Ni}(T)$. The best fits for the series $I_{i\text{-}Pr}$−M (M = Mn, Co, Ni, Zn) are shown in Fig. 4, and the corresponding exchange interaction and anisotropy parameters are reported in Table 3.

The values obtained for the exchange interaction parameter of the π-stacked radicals all along the $I_{i\text{-}Pr}$−M (M = Mn, Co, Ni, Zn) series fall below −2.4 cm^{-1}. They are in line with the value found for one of the polymorphs of $HI_{i\text{-}Pr}$ [11] where a comparable highly head-to-tail arrangement with large verdazyl−verdazyl distances known to provoke a dramatic decrease in the exchange interaction [7] was found because of the steric hindrance imposed by the isopropyl side chains of the verdazyl moiety.

4. Conclusion

The reactions of 1,5-diisopropyl-3-(4′-carboxyphenyl)-6-oxoverdazyl with divalent metal ions have led to a series of 5 compounds. Two common features appear from the analysis of the single-crystal XRD. First, the coordination to the metal ions occurs through the carboxylate moiety rather than the verdazyl one. In turn, for the $I_{i\text{-}Pr}$−M (M = Mn, Co, Ni, Zn) series where $HI_{i\text{-}Pr}$ was reacted with the acetate of the divalent metal ion, the reaction appears as a mere carboxylate exchange as previously observed for Mn$_{12}$ derivatives [19]. This statement confirms the difficulty for the verdazyl moiety to act as a monodentate ligand. Second, in all of the compounds, the π-stacking is deeply influenced by the bulky isopropyl side chains: the head-to-tail arrangement is preferred, the two interacting π-systems are not really parallel and the centroid−centroid distance between the verdazyl moieties is dramatically increased. The consequence of this structural organization onto the magnetic properties is straightforward: because of the coordination by the carboxylate group, the exchange interaction between the radical and paramagnetic metal ions is negligible, whereas the verdazyl−verdazyl interaction mediated by the π−π interactions is severely reduced.

Appendix A. Supplementary data

Supplementary data to this article can be found online at https://doi.org/10.1016/j.crci.2019.03.008.

References

[1] D. Luneau, P. Rey, Coord. Chem. Rev. 249 (23) (2005) 2591−2611.
[2] B.D. Koivisto, R.G. Hicks, Coord. Chem. Rev. 249 (23) (2005) 2612−2630.

[3] C. Train, L. Norel, M. Baumgarten, Coord. Chem. Rev. 253 (19–20) (2009) 2342–2351.

[4] L. Norel, F. Pointillart, C. Train, L.-M. Chamoreau, K. Boubekeur, Y. Journaux, A. Brieger, D.J.R. Brook, Inorg. Chem. 47 (7) (2008) 2396–2403.

[5] T.M. Barclay, R.G. Hicks, M.T. Lemaire, L.K. Thompson, Inorg. Chem. 40 (22) (2001) 5581–5584.

[6] L. Norel, L.-M. Chamoreau, Y. Journaux, O. Oms, G. Chastanet, C. Train, Chem. Commun. (17) (2009) 2381–2383.

[7] V. Chemistruck, D. Chambers, D.J.R. Brook, J. Org. Chem. 74 (5) (2009) 1850–1857.

[8] B.D. Koivisto, A.S. Ichimura, R. McDonald, M.T. Lemaire, L.K. Thompson, R.G. Hicks, J. Am. Chem. Soc. 128 (3) (2006) 690–691.

[9] J. Jornet, M. Deumal, J. Ribas-Arino, M.J. Bearpark, M.A. Robb, R.G. Hicks, J.J. Novoa, Chem. Eur J. 12 (15) (2006) 3995–4005.

[10] L. Norel, J.B. Rota, L.M. Chamoreau, G. Pilet, V. Robert, C. Train, Angew. Chem. Int. Ed. 50 (31) (2011) 7128–7131.

[11] V. Kumar, S. Shova, V. Maurel, G. Novitchi, C. Train, Eur. J. Inorg. Chem. 2018 (3) (2018) 517–524.

[12] Oxford Diffraction Ltd, CrysAlis RED Version 1.171.34.76, 2003.

[13] O.V. Dolomanov, L.J. Bourhis, R.J. Gildea, J.A.K. Howard, H. Puschmann, J. Appl. Crystallogr. 42 (2) (2009) 339–341.

[14] G.M. Sheldrick, Acta Crystallogr. C71 (2015) 3–8.

[15] P. Pascal, Ann. Chem. Phys. 19 (1910) 5–70.

[16] O. Kahn, Molecular Magnetism, VCH Publishers, Inc., New York, Weinheim, Cambridge, 1993, p. 380.

[17] C.J. O'Connor, Magnetochemistry—Advances in Theory and Experimentation, 2007, pp. 203–283.

[18] B.E. Myers, L. Berger, S.A. Friedberg, J. Appl. Phys. 40 (3) (1969) 1149–1151.

[19] R. Bagai, G. Christou, Chem. Soc. Rev. 38 (4) (2009) 1011.

[20] A.N. Sobolev, E.B. Miminoshvili, K.E. Miminoshvili, T.N. Sakvarelidze, Acta Crystallogr. Sect. E Struct. Rep. Online 59 (10) (2003) 836–837.

[21] B. Bleaney, Rev. Mod. Phys. 25 (1) (1953) 161–162.